Structure Model for Anion-Disordered Photochromic Gadolinium Oxyhydride Thin Films

Colombi, Giorgio; Cornelius, Steffen; Longo, Alessandro; Dam, Bernard

DOI
10.1021/acs.jpcc.0c02410

Publication date
2020

Document Version
Final published version

Published in
Journal of Physical Chemistry C

THE JOURNAL OF PHYSICAL CHEMISTRY C

pubs.acs.org/JPCC

Article

Structure Model for Anion-Disordered Photochromic Gadolinium Oxyhydride Thin Films

Giorgio Colombi,* Steffen Cornelius, Alessandro Longo, and Bernard Dam

Cite This: *J. Phys. Chem. C* 2020, 124, 13541−13549

Read Online

ACCESS | Metrics & More | Article Recommendations | Supporting Information

ABSTRACT: Rare-earth (RE) oxyhydride thin films prepared by reactive magnetron sputtering followed by air-oxidation show a color-neutral photochromic effect at ambient conditions within a wide composition range (REO_xH_{3-2x} where $0.5 \leq x < 1.5$). Due to the high degree of anion sublattice disorder present in these thin films, the structure models proposed for the related bulk materials are not directly applicable. Instead we use a combination of EXAFS analysis and lattice energy calculations to establish a fcc-based model linking the oxyhydrides to the related binary compounds. The oxide anions are found to occupy predominantly the tetrahedral sites in the fcc structure, which is attributed to electrostatic lattice energy minimization.

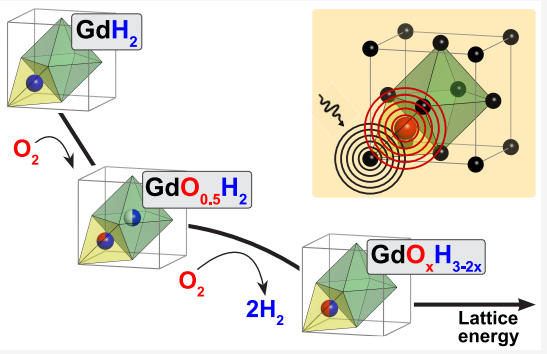

I. INTRODUCTION

Multianion compounds are an emerging class of solid state materials due to their broad spectrum of functional properties. The wide range of different anion characteristics (electronegativity, polarizability, ionic radius, etc.) offers unprecedented degrees of freedom in the design of functional materials. In contrast, the local and electronic structure of single anion compounds, such as metal oxides, is determined to a large extent by the cation chemistry.[1,2]

Previously we have shown that rare-earth based oxyhydride thin films (with RE = Sc, Y, Gd, Dy, and Er) can be synthesized via postdeposition air oxidation of RE dihydride films grown by reactive magnetron sputtering in Ar/H_2 atmosphere.[3,4] Recently, this class of compounds gained attention in view of their peculiar reversible photochromic effect and related photoconductivity.[5] Most of the recent research, however, focused at the phenomenological aspects of these functional properties while the exact chemical composition and structure of the materials remained unclear.[6−9]

The multianion nature of these films was established only in 2019, when the photochromic effect and energy gap tunability (from 2.5 to 5.5 eV) were related to the oxyhydride $RE^{3+}O_x^{2-}H_{3-2x}^{-}$ composition line which connects the trihydride (REH_3) to the oxide (RE_2O_3). To the best of our knowledge, these two binary compounds as well as the RE hydroxides are not photochromic at ambient conditions, implying that photodarkening occurs only in the presence of both O^{2-} and H^- anions.[4]

With this new compositional insight, it is worth noting that the technological potential of RE oxyhydrides thin films goes beyond applications in smart coatings for windows and sensors. Indeed, a new record for H^- ionic conductivity at intermediate temperatures was recently achieved in LaO_xH_{3-2x} powders.[10] This finding introduced simple ternary systems with a cubic structure to the group of oxyhydride ionic conductors, a class of materials otherwise dominated by far more complex layered perovskites of the Ruddlesden−Popper type, such as La_2LiHO_3, $LnSrCoO_3H_{0.7}$, $La_{2-x-y}Sr_{x+y}H_{1-x+y}O_{3-y}$ and $La_{2-x-y}Sr_{x+y}LiH_{1-x+y}O_{3-y}$.[11−14]

Given the analogous composition to LaO_xH_{3-2x}, we suppose that reactively sputtered RE oxyhydride thin films might be hydride-ion conductors as well. This property is likely tied to the still unclear mechanism of photodarkening, a process suggested to depend on the segregation of an optically absorbing phase during light exposure.[15,16] The connection between the anion mobility and the photochromic effect remains an open question, with the only hint coming from a NMR study in which the photodarkening was shown to temporarily quench the signal of the most mobile hydrogen fraction.[17]

In this context, a deeper understanding of the crystal structure of the sputtered RE−O−H films is important not only to further explore the photoinitiated diffusion processes and solid state reactions but also to assess the similarity to the other hydride-ion conductors.

Received: March 18, 2020
Revised: May 21, 2020
Published: May 26, 2020

https://dx.doi.org/10.1021/acs.jpcc.0c02410
J. Phys. Chem. C 2020, 124, 13541−13549

Table 1. Summary of the Gd−O−H Compounds Studied in This Work, Corresponding Deposition Conditions, and Key Material Properties

sample	H_2/O_2 flow (sccm)	p_{dep} (Pa)	cap (nm)	composition	E_g (eV)	ICDD-PDF	phase	d (Å)[a]	$\Delta d/d_0$ (%)
Gd metal	0/0	0.3	Pd (20)	–	–	#00-02-0864	$P6_3/mmc$	5.84	+1.4
Gd dihydride[b] (ex-situ)	0/0	0.3	Pd (20)	$GdH_{1.8}$	–	#00-50-1107	$Fm\bar{3}m$	5.33	+0.5
Gd dihydride	5/0	0.3	Al (20)	–	–	#00-50-1107	$Fm\bar{3}m$	5.36	+1.0
Gd oxyhydride	5/0	0.7	–	$GdO_{0.8}H_{1.4}$[c]	2.3	#00-50-1107	$Fm\bar{3}m$	5.41	+1.9
Gd oxide	0/1	0.3	–	Gd_2O_3	5.1	#00-12-0797	$Ia\bar{3}$	10.41	−3.9
Gd hydroxide	5/0.4	0.3	–	$GdO_{2.2}H_{1.2}$	5.3	X-ray amorphous			

[a]The experimental lattice constant (d) is derived by XRD peak fitting and ($\Delta d/d_0$) is its relative variation with respect to the reference ICDD-PDF pattern. [b]Deposition conditions refer to the pure Gd layer which is later hydrogenated in a pressure cell (1 bar of H_2 at room temperature) employing the hydrogenography method.[19] [c]Composition estimated from the EXAFS coordination numbers.

Synthesized as powders via high temperature solid state reaction between oxide and trihydride precursors, the cubic LaO_xH_{3-2x} presents a small tetragonal distortion ($P4/nmm$) in consequence of long-range anion ordering.[10] Given the strain induced by the adhesion to the substrate and the fact that reactively sputtered photochromic RE oxyhydride thin films form via a process whose driving force and kinetics are inherently different from powder synthesis, it remains unclear to which extent they share the structural (and functional) properties of the bulk RE oxyhydrides.

Until now, due to the fact that neutron diffraction is not a viable option for thin films, experimental information on the location of the H^- and O^- anions was missing.

In this work, we bridge this lack of evidence by measuring the extended X-ray absorption fine structure (EXAFS) of a set of Gd-based samples. We verify that, upon air exposure, O^{2-} anions enter the tetrahedral sites of the fcc-GdH_2 lattice. We frame this finding in a broader discussion of the lattice energy, providing in addition a qualitative explanation of the driving force behind the air-mediated formation of the photochromic RE oxyhydrides.

II. EXPERIMENTAL SECTION

II.A. Sample Preparation. Gd-based thin films of thickness ∼150 nm were prepared by reactive magnetron sputtering of a 2-in. metal target (MaTeck Germany, 99.9% purity) in a $Ar/H_2/O_2$ (5N purity) atmosphere. The deposition chamber was kept at a base pressure below 1×10^{-4} Pa. During deposition three independent mass flow controllers were used to define the composition of the gas mixture while the total deposition pressure (p_{dep}) was varied by means of a butterfly reducing valve mounted at the inlet of the pumping stage. A constant Ar flow of 35 sccm was used in combination with different H_2 and O_2 flows to synthesize samples of different chemical composition. A total power of 175 W supplied as pulsed direct current (50 kHz, 90% duty cycle) was used to sustain the plasma excitation while avoiding arcing.

All samples were grown on unheated UV-grade fused silica (f-SiO_2) and polished glassy carbon substrates. Table 1 summarizes the different binary and ternary Gd-based thin films studied in this work as well as the corresponding deposition conditions together with the key material properties. While Gd dihydride is identified by its characteristic optical transmittance window,[3,18] the oxyhydride is the only sample that shows photochromic behavior (Figure 1).[4]

A Gd dihydride reference sample (hereafter labeled as *ex-situ*) was prepared by hydrogenation of a Pd-capped (20 nm) metal layer in a pressure cell at 1 bar of H_2 at room temperature. By use of the hydrogenography method,[19] the change in optical transmittance was used to verify that the film was loaded to a H:Gd ratio above the dihydride to trihydride phase transition, followed by unloading to dihydride in air after opening of the pressure cell.

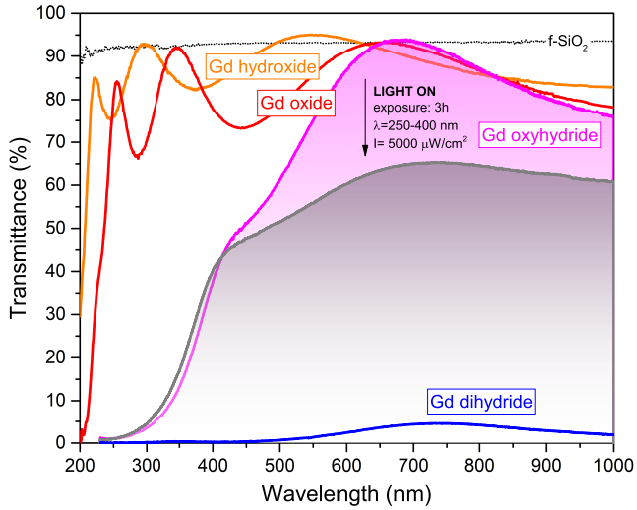

Figure 1. Transmittance of sputtered Gd−O−H thin films. Gd dihydride (blue) is a reflective metal with a transmittance window centered at ∼750 nm. Gd oxide (red) and Gd hydroxide (orange) are wide bandgap semiconductors. Gd oxyhydride (magenta) is a semiconductor with characteristic photochromic behavior; i.e., transmittance decreases by ∼30% after 3 h of UV exposure (gray). The black dotted line is the transmittance of the bare f-SiO_2 substrate.

The metallic materials (Gd and its dihydrides) were capped by a Pd or Al overlayer that was deposited without breaking the vacuum, to protect them against oxygen contamination. No protection layer was applied to the oxygen containing semiconductors.

The photochromic oxyhydride is a transparent semiconductor which forms by air-oxidation at ambient conditions from the as-sputtered metallic dihydride state. Hence, air-oxidation is an important step of oxyhydride synthesis, which depends on the film porosity and was shown to occur above a certain critical deposition pressure.[3] In the case of Gd, we find that air oxidation sets in above a value of p_{dep} = 0.7 Pa. All other films were sputtered at p_{dep} = 0.3 Pa. In contrast to the oxyhydride, the oxide as well as the hydroxide samples are already transparent upon deposition inside the vacuum chamber, suggesting that all the oxygen is incorporated in situ via the reactive O_2/H_2 atmosphere.

II.B. Sample Characterization. *Optical Properties.* The optical transmittance, $T(\lambda)$, of the wide band gap oxide and

https://dx.doi.org/10.1021/acs.jpcc.0c02410
J. Phys. Chem. C 2020, 124, 13541−13549

hydroxide samples was measured with a Perkin Elmer Lambda 900 UV−vis-NIR spectrometer with a wavelength range of 200−2500 nm. The remaining samples were investigated using a custom-built optical fiber based setup equipped with a white source (DH-2000BAL, Ocean Optics) and a silicon CCD array spectrometer (HR4000, Ocean Optics).

The transmittance of the dihydride film was measured prior to the deposition of the Al capping layer inside an oxygen free (<0.1 ppm) glovebox directly connected to the deposition chamber.

The photodarkening of the oxyhydride was initiated by a low pressure Hg UV-lamp (Herolab GmbH) with an emission range of 245−400 nm and an integrated irradiance of 5000 μW cm^{-2}, which is comparable to that of the sun (4610 μW cm^{-2}) in the same spectral range.[20]

The optical bandgap, E_g, was determined using the Tauc plot method with an estimated error of about ΔE_g = 0.1 eV.[21,22]

Chemical Composition. The absolute composition of the samples was determined by a combination of Rutherford backscattering (RBS) and Elastic recoil detection (ERD) ion beam techniques with an estimated accuracy of 1 at. %. Given the intricacy of the topic, the reader is referred to the original paper for further details.[4] Note that ion beam analysis was crucial to clearly distinguish the Gd oxide, oxyhydride, and hydride samples.

X-ray Diffraction. Parallel-beam X-ray diffraction (XRD) data were recorded on a Bruker D8 Discover diffractometer equipped with a Cu tube (λ = 1.5406 Å) combined with a 40 mm Goebel mirror as well as a 0.2° equatorial Soller slit mounted to a LynxEye XE energy dispersive linear detector.

All samples were initially measured in symmetric geometry (2:1), where the incidence angle equals half of the scattering angle (ω = 2Θ/2). The presence of preferential orientation was assessed by rocking curves around the main peaks (scanning ω at fixed 2Θ).

Lattice constants were determined from the main peak positions obtained by fitting a constrained double Pseudo-Voigt function (to account for the Cu K$\alpha_{1/2}$ doublet) to the experimental data. The resulting values were also corrected for instrumental deviations in scattering angle, 2Θ, by measuring a NIST certified powder standard (SRM-1976b corundum Al_2O_3) in the same geometry.

Given the large FWHM values observed for the sputtered polycrystalline films of this work, the uncertainty of the lattice constants is estimated to be ±0.01 Å.

X-ray Absorption Spectroscopy. Gd-L3 X-ray absorption spectra were collected at the EXAFS stations (bending-magnets no. 26 and no. 14) of the Dutch−Belgian beamline (DUBBLE) at the European Synchrotron Radiation Facility (ESRF, Grenoble France). The energy, E, of the X-ray beam was controlled by a Si(111) double crystal monocromator with a resolution of $\Delta E/E \sim 1 \times 10^{-4}$. Across the whole measurement range, from 7043 eV (200 eV below the Gd-L3 edge) to 7820 eV (just below the Gd-L2 edge), the accuracy of the energy calibration was confirmed to be within 0.25 eV by measuring the K-edge of Co (7112 eV), Fe (7708.9 eV), and Ni (8332.8 eV) reference foils. The thin films were measured in fluorescence geometry at an incidence angle of ∼35° and an exit angle of ∼60°, defined by the orientation of the sample and the position of the ORTEC IGLET 9-element Ge detector, respectively.

The metallic samples and the photochromic oxyhydride were measured at 80 K in a liquid nitrogen cryostat. In contrast, given the dominant site disorder, oxide and hydroxide samples were measured at room temperature in air.

Taking into consideration the Gd absorption cross section, the thickness of the films and their density, we estimate negligible effects of self-absorption (Figure S4); therefore no correction is performed during data treatment.[23] After background subtraction of the raw data, EXAFS oscillations, $\chi(E)$, have been expressed in terms of the photoelectron wavenumber ($k = \sqrt{2m_eE}/\hbar$), $\chi(k)$, and Fourier transformed (FT) to the direct space, $\chi(r)$, for a more intuitive interpretation. To compensate for the diminishing amplitude at high-k, a weighting factor of k^2 is adopted prior to the FT. In the framework of the single scattering (SS) and multiple-scattering (MS) path expansion, the weighted Fourier transformed data, $FT[k^2 \times \chi(k)]$, is finally fitted according to the EXAFS equation (Supporting Information, section II.A):

$$\chi(k) = {S_0}^2 \sum_j \frac{N_j}{k{r_j}^2} f_j(k, r_j) e^{-2\sigma_j^2 k^2} e^{-2r_j/\lambda_j(k)} \sin(2kr_j + \delta_j(k)) \quad (1)$$

For each jth-shell the amplitude, $f_j(k, r_j)$, phase shift, δ_j, and photoelectron mean free path, $\lambda_j(k)$, are calculated ab initio with the FEFF9 code.[24,25] The coordination number, N_j, the effective distance, r_j, and the Debye−Waller factor, σ_j, are taken instead as fitting parameters (sometimes constrained). A fourth variable, the energy shift, $e_{0,j}$, is added to account for experimental energy offsets and for the possible mismatch with the ab initio calculation. Due to the absence of references, the amplitude reduction factor, S_0, is taken as equal to 1, possibly leading to a systematic, small underestimation of the coordination numbers.[26,27]

Data processing including averaging of scans, background subtraction, forward Fourier transform of the k^2-weighted data, and fitting was performed using the Viper software.[28]

The errors have been estimated by the correlation map between parameters and reflect a confidence interval of 2σ = 68%.

II.C. Madelung Energy Calculation. The Madelung energies of Gd−O−H structures have been calculated using MADEL, an applet called in by VESTA.[29] The code employs the Fourier method, for which the radius of an ionic sphere was chosen to be slightly smaller than the shortest interatomic distance while the reciprocal space range was set to 6 Å^{-1}. The convergence of the Madelung energy upon variation of both parameters was verified.

III. RESULTS

III.A. Optical Properties and Photochromism. Due to the mixed H_2/O_2 reactive atmosphere and possible air-oxidation, a wide range of binary and ternary Gd−O−H compounds may result from reactive magnetron sputter deposition.[3,4] Optical transmittance spectra were used to verify the electronic state of each of the Gd−O−H thin films (Figure 1).

Gd dihydride films appear as optically thick metals with the exception of a region of weak transmittance in the red part of the visible spectrum. This transmittance window is a characteristic property of the RE dihydrides[3,30] and is known to arise due to a combination of a weak interband and free electron absorption close to the plasma frequency.[18] Gd oxide and hydroxide are both wide bandgap semiconductors with indirect optical bandgaps of 5.1 and 5.3 eV respectively.

https://dx.doi.org/10.1021/acs.jpcc.0c02410
J. Phys. Chem. C 2020, 124, 13541−13549

Finally, the oxyhydride is the photochromic semiconductor that, after exposure to UV light for 3 h, shows an average contrast (ΔT) of 31.5% in the 450−1000 nm wavelength range. By comparing to the trend in band gap variation with respect to REO_xH_{3x-2} oxyhydride composition, the measured band gap value (2.3 eV) suggests that the oxyhydride studied in this work belongs to the oxygen poor region ($0.5 < x < 1$) of the composition range.[4]

Additional information about the semiconducting samples can be inferred from the typical thin film interference patterns in the long wavelength part of the transmittance spectra.[31] The fact that the interference maxima reach the transmittance of the bare f-SiO_2 substrate implies that the sub band gap absorption, i.e., due to optically active defects, is negligible. Moreover, the value of the interference minima is linked to the difference in refractive index between film and substrate. The data in Figure 1 suggests that the refractive index decreases with increasing oxygen content, x, i.e., from oxyhydride to oxide to hydroxide, which is in good agreement with our earlier work[4] and a recent study by You et al.[7]

III.B. Crystalline Structure. XRD is employed to probe the long-range crystal structure and to determine the lattice constants of the Gd−O−H thin films, as shown in Figure 2.

The phase of each compounds was identified by comparison to the ICDD-PDF patterns reported in Table 1. The Gd metal is the only film showing hexagonal structure and its two main peaks at 28.8° and 30.6° match with the (100) and (002) crystal planes of the hcp-$P6_3/mmc$ pattern (#00-02-0864).

In agreement with our previous studies, the diffraction patterns of the remaining films show fcc symmetry, best matched by the $Fm\bar{3}m$ pattern of GdH_2 (#00-50-1107).[3,4] Due to the limited number of reflections and their large FWHM it is not possible to exclude the small degree of tetragonal distortion which was reported for the similar anion-ordered LnOH ($c/\sqrt{2}a = 0.997$) and $LnO_{0.5}H_2$ ($c/\sqrt{2}a = 0.999$) oxyhydrides.[10,32]

The rocking curve FWHM is a relative measure of the degree of out-of-plane preferential orientation of thin films. According to the rocking curves shown in the insets of Figure 2, we find that the Gd metal film has a preferential out-of-plane orientation along the hcp c-axis. This texture is maintained during ex-situ hydrogenation of Gd to GdH_2, i.e. the phase transition occurs in such way that the hcp c-axis (002) is parallel to fcc space diagonal (111). This structure evolution is in agreement with the well documented case of hydrogenation of Y to YH_2.[4,33] In contrast, the (in situ) reactively sputtered GdH_2 film has no significant (111) texture, which is also indicated by the absence of the (222) peak. Similarly, the photochromic Gd oxyhydride is not textured either. In case of Gd oxide, we would expect the thermodynamically stable cubic bixbyite structure ($Ia\bar{3}$, #00-12-0797), which is essentially a distorted fcc structure with ordered oxygen vacancies.[34,35] In the XRD pattern, this results in the appearance of (weak) superstructure peaks in addition to the main fcc peaks, as we have reported recently for the cases of reactively sputtered Y_2O_3 and Sc_2O_3 films.[4] Here, these superstructure peaks are absent in the Gd oxide XRD pattern (Figure 2), which is probably a consequence of the substantial (111) texture of this sample that suppresses the signal from other crystal planes. Therefore, we identify the structure of the Gd_2O_3 as bixbyite despite the missing superstructure peaks.

Table 1 reports the determined lattice constants (d) and their variation with respect to the reference patterns. While the

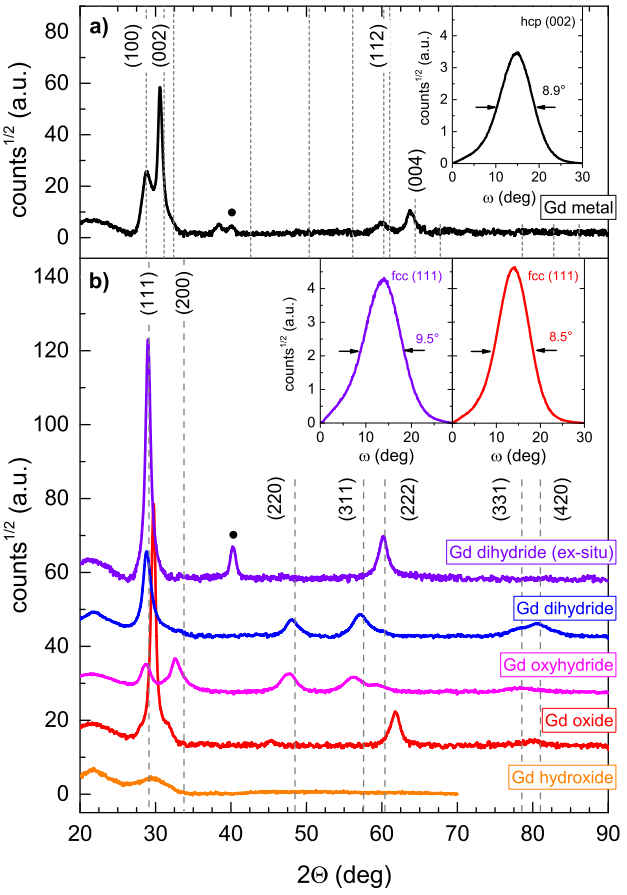

Figure 2. XRD patterns of the polycrystalline Gd−O−H thin films. (a) Gd metal is ascribed to the hexagonal $P6_3/mmc$ pattern #00-02-0864 (dotted vertical lines). (b) Gd dihydride, oxyhydride, and oxide have cubic symmetry and are shown versus the $Fm\bar{3}m$ pattern #00-50-1107 of the GdH_2 (dashed vertical lines). The lattice constants of all compounds are reported and compared to the respective ICDD-PDF reference patterns in Table 1. The peaks indexed with • are due to the Pd capping while the broad feature centered at $2\Theta \sim 22°$ is due to scattering by the f-SiO_2 substrate. The inserts show the rocking curves of the prominent peaks of the textured samples.

oxide appears compressed along the (111) direction, all the other samples show a slight expansion, which is typical for sputtered thin films.[3] Notably, the lattice constants of the hydrogenated ex-situ dihydride (5.33 Å), sputtered dihydride (5.36 Å), and oxyhydride (5.41 Å) present the increasing trend already reported for Gd, Dy, Y and Er based RE−O−H compounds.[3]

III.C. EXAFS: Local Structure. EXAFS was used to investigate the Gd local environment and therefore understand the location of oxygen in the Gd−O−H structures. In Figure 3, we show the Gd-L3 EXAFS data and their best fit up to the 2nd shell. The corresponding fitting parameters and their uncertainty are reported in Table 2.

All the polycrystalline thin films were fitted with models constructed from the insight inferred from XRD. To fit the EXAFS signal of the X-ray amorphous hydroxide, we tested all the relevant space groups of the ICDD-PDF database (Table S3), finding however that the best fit parameters were always equal within error. In Table 2 we report those corresponding to the monoclinic $P2_1/m$ (a = 4.39 Å, b = 3.75 Å, c = 6.13 Å) oxyhydroxide GdO(OH), which is the hydroxide-like com-

https://dx.doi.org/10.1021/acs.jpcc.0c02410
J. Phys. Chem. C 2020, 124, 13541−13549

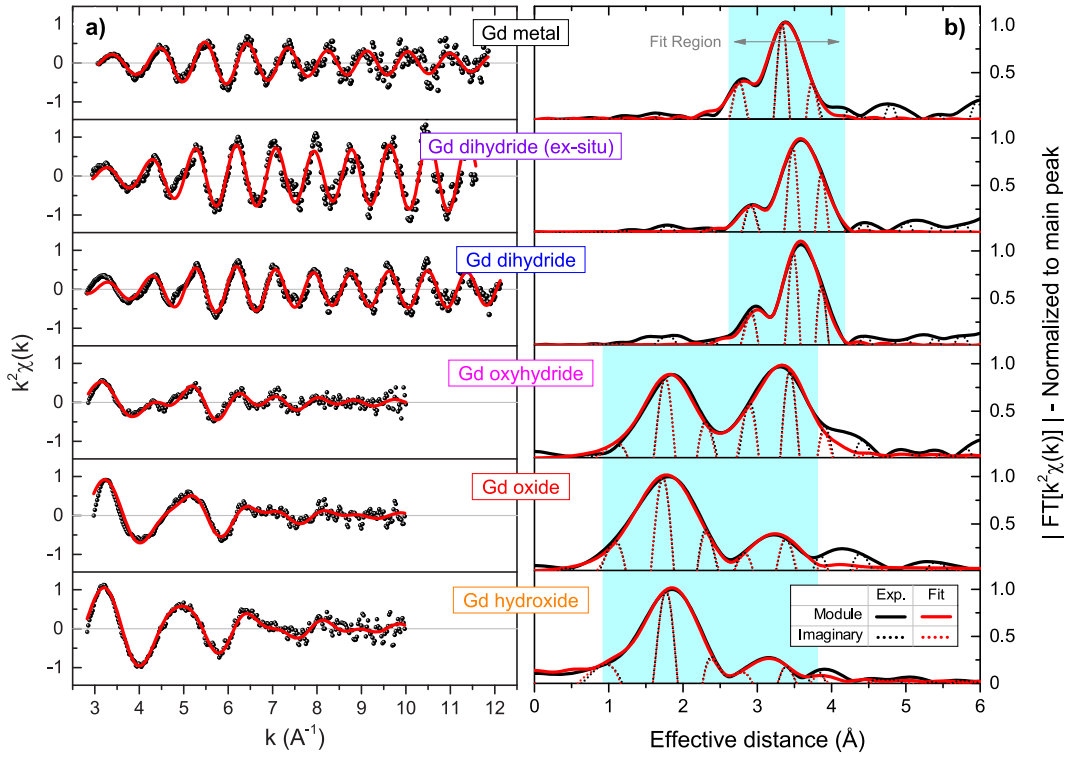

Figure 3. (a) k^2-weighted EXAFS data and (b) corresponding Fourier transform of the reactively sputtered Gd−O−H thin films. The red curves correspond to the best fits as done in real space for the shells indicated by the light blue background.

Table 2. Results Obtained from the EXAFS Fitting of the Gd−O−H Thin Films[a]

Path	N (atoms)	r (Å)	σ (10^{-3} Å^2)	e_0 (eV)
Gd metal (80 K)			***R* = 3.0%**	***ν* = 2**
Gd−Gd #1	5.2(5)	3.55(1)	5.2(4)	2.8(8)
Gd−Gd #2	4.9(5)	3.67(1)	6.6(4)	
Gd dihydride (ex-situ) (80 K)			***R* = 3.9%**	***ν* = 7**
Gd−Gd #1	11.9(4)	3.737(2)	5.2(1)	3.0(1)
Gd dihydride (80 K)			***R* = 6.0%**	***ν* = 6**
Gd−Gd #1	10.3(1)	3.745(1)	7.4(1)	3.5(3)
Gd oxyhydride (80 K)			***R* = 5.8%**	***ν* = 6**
Gd−O #1	2.5(2)	2.305(6)	13(3)	4.4(3)
Gd−Gd #1	9.3(5)	3.677(6)	18(1)	
Gd oxide (RT)			***R* = 5.0%**	***ν* = 5**
Gd−O #1	5.3(4)	2.27(1)	14(1)	3.2(9)
Gd−Gd #1	5.7(9)	3.63(2)	13(4)	
Gd hydroxide (RT)			***R* = 4.4%**	***ν* = 6**
Gd−O #1	6.4(6)	2.34(1)	14(1)	1.8(5)
Gd−Gd #1	4.1(7)	3.65(2)	13(3)	

[a]For each sample, R is the final value of the minimized function while ν is the difference between the number of independent data points and free variables. The error on the last significant figure is reported in round brackets behind each value.

pound whose formula unit best matches the experimental composition of the sputtered film.

The contribution of the H was neglected because it is insignificant compared to that of the oxygen atoms, as is visually evident when comparing the spectra of the metallic samples to those of the oxygen containing semiconductors.

The fitting results show that in all cases the oxygen gives rise to a coordination shell at a distance of ∼2.3 Å, which corresponds to a path of single scattering between the Gd atoms and the oxygen located in the tetrahedral sites of the Gd lattice. In contrast, the occupation of octahedral sites would appear at ∼2.7 Å.

While such distance matches the expectation for oxide and hydroxide, the case of the photochromic sample is less trivial: given the stoichiometry of a H-rich oxyhydride (REO_xH_{3-2x} with $0.5 \leq x < 1$), it follows that in each unit cell there are more anions than available tetrahedral sites. The fact that the first coordination shell occurs at 2.305(6) Å implies that the oxygen incorporated upon air exposure enters the structure into the tetrahedral sites, displacing a fraction of H^- anions to a different location. Constraining the distance of the O shell according to an ideal fcc unit led to a poor fit, suggesting that in the oxyhydride the O^{2-} anions are slightly displaced from the exact center of the interstitial sites. Besides this distortion, which is small (∼13%) compared to the Gd−O bond length, all distances are consistent with the symmetry of the space group of each sample.

The Gd−O #1 coordination numbers of the semiconductors follow the trend of increasing oxygen concentration from oxyhydride (2.5) to oxide (5.3) to hydroxide (6.4), as qualitatively shown by the peak ratios of Figure 3b. All the coordination numbers indicate a minor under-coordination with respect to the ideal bulk compounds, following from the assumption on S_0^2 and possibly reflecting the defective structure of reactively sputtered films and their finite grain size.[36] On the basis of the coordination of the oxyhydride, $N_{Gd-O\#1}$ = 2.7(2) and $N_{Gd-Gd\#2}$ = 9.9(8), we estimate an oxygen fraction of x = 0.8(1) and therefore the chemical

https://dx.doi.org/10.1021/acs.jpcc.0c02410
J. Phys. Chem. C 2020, 124, 13541−13549

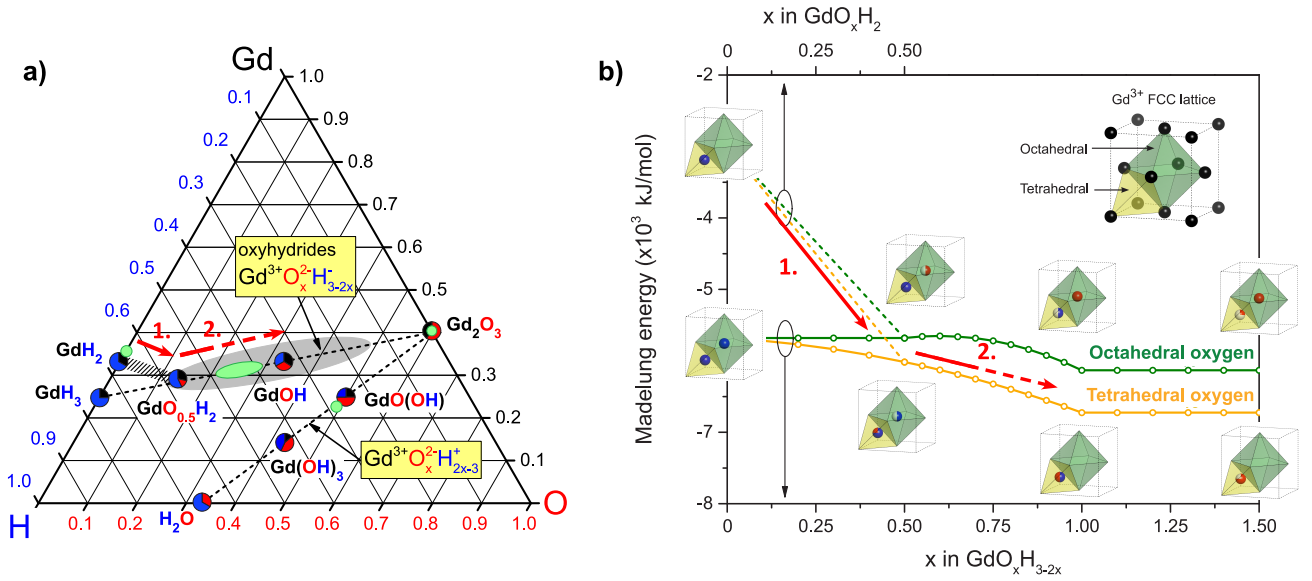

Figure 4. (a) Ternary Gd−O−H chemical composition diagram. The dashed lines indicate compositions where elements are in the same charge state: M^{3+}, O^{2-}, and H^- for the oxyhydride and M^{3+}, O^{2-}, and H^+ for the hydroxide-like compounds. The bigger and labeled circles mark the ideal stoichiometric compounds and are colored according to the fraction of Gd (black), O (red), and H (blue). The experimental chemical composition of the thin films studied in this work is indicated in green, where the circles are obtained from ion beam analysis while the larger ellipse is estimated from the EXAFS coordination numbers of the oxyhydride sample. (b) Madelung energy evaluated along the oxyhydride composition line assuming oxygen incorporation into the tetrahedral (yellow line) and octahedral (green line) sites, respectively. The inserts show the site occupation in the two cases for selected structures (GdH_3, $GdO_{0.5}H_2$, GdOH, and Gd_2O_3). In both panels the red arrows denote the hypothesized two-step pathway of air-mediated oxidation that leads to the formation of the oxyhydride from the in situ sputtered dihydride (eqs 2a and 2b).

formula $GdO_{0.8}H_{1.4}$ (Supporting Information), which corresponds, as expected from the low E_g, to the H-rich end of the photochromic oxyhydride composition range.

From the Debye−Waller factors we conclude that the sputtered dihydride is more disordered than the ex-situ hydrogenated one while the oxyhydride is the most disordered structure of all, most likely because of the higher deposition pressure together with the large site disorder and strain induced by post deposition air-oxidation.

As an additional sign of consistency, we note that the Gd-L3 edge progressively shifts toward higher energies reflecting the increasing oxidation state of the Gd ions from metal to dihydride (Gd^{2+}) to oxide (Gd^{3+}) and hydroxide (Gd^{3+}) (Figure S3).

IV. DISCUSSION

IV.A. GdH_2 Air-Oxidation and Resulting Oxyhydride Structure. The recently established RE−O−H phase diagram suggests that the formation of GdO_xH_{3-2x} oxyhydrides via air oxidation formally follows a two-step reaction path (visualized by the arrows in Figure 4):[4]

$$GdH_2 + \frac{1}{4}O_2 \rightarrow GdO_{0.5}H_2 \quad (2a)$$

$$GdO_{0.5}H_2 + \frac{2x-1}{4}O_2 \rightarrow GdO_xH_{3-2x} + \frac{2x-1}{2}H_2\uparrow \quad (2b)$$

The EXAFS radial distribution of the oxyhydride reveals that the oxygen sits at 2.305(6) Å from the Gd atoms, therefore occupying the tetrahedral sites of the cation lattice.

Such coordination appears counterintuitive for two reasons. First, the oxygen enters into a structure where the tetrahedral sites are already filled by H^- ions, which therefore need to be displaced. Second, even though O^{2-} and H^- ions have fairly similar radii ($R_{O^{2-}} \sim 140$ pm, $R_{H^-} \sim 120 - 150$ pm), the first is far less polarizable than the second.[1] It follows that the oxygen insertion is accompanied by mechanical stress, as confirmed by the expanded lattice of the oxyhydrides compared to the dihydrides.[3]

The tetrahedral sites of the fcc structure are smaller than the octahedral ones, therefore it is not a principle of size exclusion that guides the oxygen incorporation. On the contrary, given the largely ionic nature of the compound, the driving force behind the oxidation process is most likely of electrostatic nature.

In this framework, the preferred occupation of the tetrahedral sites by the oxide ions can be explained by a difference in lattice enthalpy, i.e., the energy released when ions are brought together and spatially combined to form the compound.

Neglecting any covalency to the bonding and the finite size of the atoms, the lattice enthalpy rewrites as (minus) the coulomb energy (Madelung energy, E_M). Values of E_M for compounds that belong to the GdO_xH_2 and GdO_xH_{3-2x} composition lines are shown in Figure 4b. The first (dashed) line spans from GdH_2 to $GdO_{0.5}H_2$ and refers to the absolute composition of the compound as Gd is progressively oxidized and the metal to insulator transition occurs near $x = 0.5$ (eq 2a). The second (full) line connects GdH_3 to Gd_2O_3 and includes the region of photochromism: $0.5 < x < 1.5$ (eq 2b).

The evaluation of E_M was repeated for two cases, hereafter referred to as *octahedral oxygen* (O_{oct}) and *tetrahedral oxygen* (O_{tet}) respectively. In the O_{oct} case, the O^{2-} anions are assumed to reside in the bigger octahedral sites, while in the O_{tet} case they are placed in the tetrahedral sites and an equal number of H^- ions are displaced to octahedral positions. To focus on the contribution of the anions positioning only, the

https://dx.doi.org/10.1021/acs.jpcc.0c02410
J. Phys. Chem. C 2020, 124, 13541−13549

fcc lattice of the cations was kept constant and approximated for all structures to the one of the oxyhydride ($Fm\bar{3}m$, a = 5.41 Å).

In its simplicity, this model provides a qualitative explanation of the main driving force behind the dihydride oxidation and the preference of oxygen for the smaller tetrahedral sites. Indeed, there is not a single composition for which octahedral oxygen would lead to an energy gain with respect to a tetrahedral occupancy. This is also predicted by the so-called *radius-ratio* rule, which is a direct consequence of the lattice energy and can be summarized as follows: if the radii allow, the most favorable structure for an ionic compound is the one that maximizes the coordination of the most charged constituents.[37] In our case, the Gd^{3+} is 8-fold coordinated by tetrahedral sites and only 6-fold coordinated by the octahedral ones, which moreover are further apart in space.

To understand the trends shown in Figure 4b, one should consider that the Madelung energy is an infinite (but convergent) summation which runs over all the ions that make the crystal. In practice, to account for partial occupancies and for the mixed anion sublattice, it is convenient to define the average charge for each equivalent crystallographic site (tetrahedral, octahedral, etc.) and to sum over all the crystal site positions. When the anion substitution is not accompanied by a variation of the average charge in any of the crystallographic sites, E_M does not change ($x \leq 0.5$ for O_{oct} case and $x \geq 1$ for both cases). In the O_{tet} case, from $x = 0$ to $x = 1$, the absolute value of the Madelung energy increases as the charge is effectively displaced from the octahedral to the more advantageous tetrahedral sites. In contrast, for the O_{oct} case the energy gain due to a reduced anion−anion repulsion is counterbalanced by the charge displacement toward the less advantageous octahedral sites: from these two opposing contributions E_M shows a weak peak in the region $0.5 \leq x \leq 1.5$.

We stress that the results of our calculation, after correction with the repulsive (constant) term of the Born-Landé equation, match the experimental lattice energy of REH_2 (fcc) and RE_2O_3 (bixbyite) reference compounds (with RE = Y, Gd) within 10% of error. However, due to the challenges that thin films pose to the measurement of thermodynamic quantities, the ionic character of sputtered RE oxyhydrides has never been verified via the Born−Haber cycle. Nevertheless, the electronegativities of the constituting atoms (Gd = 1.2, O = 3.44, H = 2.20 in Pauling scale) and the sizeable optical band gap along the whole composition range[4] point toward bound electronic states. Similar arguments have been originally raised to justify a local description in binary LaH_3 and YH_3 trihydrides and an extension to the ternary REO_xH_{3-2x} appears well-founded.[38,39] On this basis, the ionic picture seems to be a qualitatively valid approximation for the RE oxyhydrides. In addition, we notice that these considerations are not new in the context of mixed-anion compounds and it has already been shown that the Madelung energy is able to capture the essential features of the valence band structure of complex bismuth oxyhalide layered peroskites.[40]

IV.B. The Anion-Disordered Structure Model. The EXAFS data and the lattice energy minimization arguments of this work verify the preference of the anions for the tetrahedral sites, substantiating the generalized structural model reported in Figure 5. Here, the structural evolution along the GdO_xH_2 and GdO_xH_{3-2x} composition lines is described in terms of an anion-disordered unit based on the fluorite fcc structure with variable lattice constant.

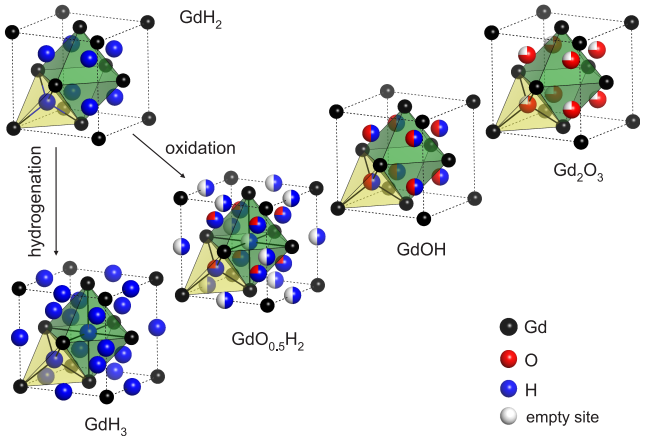

Figure 5. Generalized crystal structure evolution of rare-earth oxyhydrides with different H^-/RE and O^{2-}/RE ratios based on the fcc-fluorite ($Fm\bar{3}m$) structure motif. Anion sublattice disorder is visualized by multicolored spheres in terms of partial occupancy of tetrahedral (yellow polygon) and octahedral (green polygon) sites. The arrows indicate metal−insulator transitions. Figure adapted from Cornelius et al.[4] Copyright 2019 American Chemical Society.

In this framework, air-oxidation of the as-deposited REH_2 films to the $REO_{0.5}H_2$ involves displacement of hydride ions from tetrahedral to octahedral sites as the O^{2-} ions take their place and the RE cation is oxidized from RE^{2+} to RE^{3+} (eq 2a). This step also results in a well documented lattice expansion with respect to the initial dihydride.[3] Further oxygen inclusion is not accompanied by a change in oxidation states but rather requires the release of hydrogen to maintain charge neutrality (eq 2b).

We notice that several groups reported ordering of the anion sublattice in RE oxyhydrides (RE = Y, Ln, Cr, Pr, Nd) prepared via high temperature/pressure chemical routes.[10,41−43] In addition, a variety of anion-ordered YO_xH_{3-2x} polymorphs with different O:H ratios were hypothesized by density functional theory.[44] However, the air mediated postoxidation of the reactively sputtered REH_2 does not proceed under thermodynamic control: as a result, oxyhydride films produced in this way (with RE = Sc, Y, Gd, Dy, Er) do not show any obvious structural variation from the cubic $Fm\bar{3}m$ symmetry.[3,4,45] This suggests a substantial absence of anion ordering in consequence of the initial structure of the dihydride layer as well as the insufficient energy for structural rearrangement (via diffusion) at room temperature. Nevertheless, we cannot exclude a certain degree of anion-ordering and tetragonality. The small displacement of the oxygen ions from the exact center of the tetrahedral sites, similarly observed in the anion-ordered LaO_xH_{3-2x} powders,[10] might indeed be an indication of the onset of anion ordering in the Gd oxyhydride film investigated in this work.

In any case, our simplified description provides an insightful framework whose added value is the ability to estimate the fraction of empty interstitial sites as a function of the H:O ratio along the REO_xH_{3-2x} oxyhydride composition line. In the region of H-rich compounds ($0 < x \leq 1$), the occupancy, g, of the octahedrals diminishes linearly from $g_{oct} = 1$ in the REH_3 to $g_{oct} = 0$ in the REOH. For O-rich compositions ($1 \leq x \leq 1.5$), the tetrahedrals get linearly depleted from $g_{tet} = 1$ in the REOH to $g_{tet} = 0.75$ in the RE_2O_3 oxide.

https://dx.doi.org/10.1021/acs.jpcc.0c02410
J. Phys. Chem. C 2020, 124, 13541−13549

Taking into account that the fraction and the kind of free sites strongly influence the ionic/electronic conductivity, and most likely the photochromic effect as well, we believe that such insight will act as a guideline for designing RE oxyhydrides with optimally tuned functional properties.

V. CONCLUSION

Multianion compounds are a largely unexplored class of widely tunable functional materials. In this context, RE-based oxyhydrides stand out because of their unique photochromic properties and the possibility of synthesizing them via air-oxidation of reactively sputtered RE dihydride thin films.

In this work we investigated the local structure of various Gd−O−H compounds, where the increasing oxygen content is reflected by consistent trends of decreasing refractive index and increasing energy gap, Gd−O EXAFS coordination number and XANES edge position.

The EXAFS analysis presented here shows that the oxygen substitutes for hydrogen at the tetrahedral interstitial sites of the fcc Gd lattice.

Calculation of the Madelung energy suggests that the preference of the oxide ions for the tetrahedral sites is due to a favorable electrostatics as compared to the octahedral occupancy. Furthermore, we identify in the lattice energy the main driving force for the oxyhydride formation by air-oxidation of dihydride films.

Still, much remains unknown about the degree of anion ordering, the hypothesized H^- conductivity, and the physical mechanism behind the photochromic effect of the RE oxyhydrides. The structural insight provided here may serve as valuable starting point for further experimental and computational work.

■ ASSOCIATED CONTENT

Supporting Information

The Supporting Information is available free of charge at https://pubs.acs.org/doi/10.1021/acs.jpcc.0c02410.

XANES, further details on EXAFS analysis, and XRD references from the ICDD database (PDF)

■ AUTHOR INFORMATION

Corresponding Author

Giorgio Colombi − *Materials for Energy Conversion and Storage, Department of Chemical Engineering, Delft University of Technology, NL-2629HZ Delft, The Netherlands;* orcid.org/0000-0001-6424-7684; Email: G.Colombi@tudelft.nl

Authors

Steffen Cornelius − *Materials for Energy Conversion and Storage, Department of Chemical Engineering, Delft University of Technology, NL-2629HZ Delft, The Netherlands;* orcid.org/0000-0002-0358-7287

Alessandro Longo − *European Synchrotron Radiation Facility, The European Synchrotron, 38000 Grenoble, France; Istituto per lo Studio dei Materiali Nanostrutturati (ISMN)-CNR, UOS Palermo, 90146 Palermo, Italy*

Bernard Dam − *Materials for Energy Conversion and Storage, Department of Chemical Engineering, Delft University of Technology, NL-2629HZ Delft, The Netherlands;* orcid.org/0000-0002-8584-7336

Complete contact information is available at: https://pubs.acs.org/10.1021/acs.jpcc.0c02410

Notes

The authors declare no competing financial interest.

■ ACKNOWLEDGMENTS

The authors thank Dr. Roelof van Silfhout for facilitating access to ESRF-BM14; Herman Schreuders and Ben Norder for maintaining the sputtering and XRD systems; and Diana Chaykina, Nienke Firet, and Fahimeh Nafezarefi for the insightful discussions.

■ REFERENCES

(1) Kageyama, H.; Hayashi, K.; Maeda, K.; Attfield, J. P.; Hiroi, Z.; Rondinelli, J. M.; Poeppelmeier, K. R. Expanding frontiers in materials chemistry and physics with multiple anions. *Nat. Commun.* **2018**, *9*, 772.

(2) Kobayashi, Y.; Hernandez, O.; Tassel, C.; Kageyama, H. New chemistry of transition metal oxyhydrides. *Sci. Technol. Adv. Mater.* **2017**, *18*, 905−918.

(3) Nafezarefi, F.; Schreuders, H.; Dam, B.; Cornelius, S. Photochromism of rare-earth metal-oxy-hydrides. *Appl. Phys. Lett.* **2017**, *111*, 103903.

(4) Cornelius, S.; Colombi, G.; Nafezarefi, F.; Schreuders, H.; Heller, R.; Munnik, F.; Dam, B. Oxyhydride nature of rare-earth-based photochromic thin films. *J. Phys. Chem. Lett.* **2019**, *10*, 1342−1348.

(5) Mongstad, T.; Platzer-Björkman, C.; Maehlen, J. P.; Mooij, L. P.; Pivak, Y.; Dam, B.; Marstein, E. S.; Hauback, B. C.; Karazhanov, S. Z. A new thin film photochromic material: oxygen-containing yttrium hydride. *Sol. Energy Mater. Sol. Cells* **2011**, *95*, 3596−3599.

(6) You, C. C.; Mongstad, T.; Maehlen, J. P.; Karazhanov, S. Engineering of the band gap and optical properties of thin films of yttrium hydride. *Appl. Phys. Lett.* **2014**, *105*, 031910.

(7) You, C. C.; Mongstad, T.; Marstein, E. S.; Karazhanov, S. Z. The dependence of structural, electrical and optical properties on the composition of photochromic yttrium oxyhydride thin films. *Materialia* **2019**, *6*, 100307.

(8) Montero, J.; Martinsen, F.; Lelis, M.; Karazhanov, S.; Hauback, B.; Marstein, E. Preparation of yttrium hydride-based photochromic films by reactive magnetron sputtering. *Sol. Energy Mater. Sol. Cells* **2018**, *177*, 106−109.

(9) Nafezarefi, F.; Cornelius, S.; Nijskens, J.; Schreuders, H.; Dam, B. Effect of the addition of zirconium on the photochromic properties of yttrium oxy-hydride. *Sol. Energy Mater. Sol. Cells* **2019**, *200*, 109923.

(10) Fukui, K.; Iimura, S.; Tada, T.; Fujitsu, S.; Sasase, M.; Tamatsukuri, H.; Honda, T.; Ikeda, K.; Otomo, T.; Hosono, H. Characteristic fast H^- ion conduction in oxygen-substituted lanthanum hydride. *Nat. Commun.* **2019**, *10*, 2578.

(11) Kobayashi, G.; Hinuma, Y.; Matsuoka, S.; Watanabe, A.; Iqbal, M.; Hirayama, M.; Yonemura, M.; Kamiyama, T.; Tanaka, I.; Kanno, R. Pure H^- conduction in oxyhydrides. *Science* **2016**, *351*, 1314−1317.

(12) Watanabe, A.; Kobayashi, G.; Matsui, N.; Yonemura, M.; Kubota, A.; Suzuki, K.; Hirayama, M.; Kanno, R. Ambient pressure synthesis and H^- conductivity of $LaSrLiH_2O_2$. *Electrochemistry* **2017**, *85*, 88−92.

(13) Matsui, N.; Kobayashi, G.; Suzuki, K.; Watanabe, A.; Kubota, A.; Iwasaki, Y.; Yonemura, M.; Hirayama, M.; Kanno, R. Ambient pressure synthesis of La_2LiHO_3 as a solid electrolyte for a hydrogen electrochemical cell. *J. Am. Ceram. Soc.* **2019**, *102*, 3228−3235.

(14) Iwasaki, Y.; Matsui, N.; Suzuki, K.; Hinuma, Y.; Yonemura, M.; Kobayashi, G.; Hirayama, M.; Tanaka, I.; Kanno, R. Synthesis, crystal structure, and ionic conductivity of hydride ion-conducting Ln_2LiHO_3 (Ln = La, Pr, Nd) oxyhydrides. *J. Mater. Chem. A* **2018**, *6*, 23457−23463.

(15) Montero, J.; Karazhanov, S. Z. Spectroscopic ellipsometry and microstructure characterization of photochromic oxygen-containing yttrium hydride thin yilms. *Phys. Status Solidi A* **2018**, *215*, 1701039.
(16) Montero, J.; Martinsen, F. A.; García-Tecedor, M.; Karazhanov, S. Z.; Maestre, D.; Hauback, B.; Marstein, E. S. Photochromic mechanism in oxygen-containing yttrium hydride thin films: An optical perspective. *Phys. Rev. B: Condens. Matter Mater. Phys.* **2017**, *95*, 201301.
(17) Chandran, C. V.; Schreuders, H.; Dam, B.; Janssen, J. W. G.; Bart, J.; Kentgens, A. P. M.; van Bentum, P. J. M. Solid state NMR studies of the photochromic effects of thin films of oxygen containing yttrium hydride. *J. Phys. Chem. C* **2014**, *118*, 22935.
(18) van Gogh, A. T. M.; Nagengast, D. G.; Kooij, E. S.; Koeman, N. J.; Rector, J. H.; Griessen, R.; Flipse, C. F. J.; Smeets, R. J. J. G. A. M. Structural, electrical, and optical properties of $La_{1-z}Y_zH_x$ switchable mirrors. *Phys. Rev. B: Condens. Matter Mater. Phys.* **2001**, *63*, 195105.
(19) Gremaud, R.; Slaman, M.; Schreuders, H.; Dam, B.; Griessen, R. An optical method to determine the thermodynamics of hydrogen absorption and desorption in metals. *Appl. Phys. Lett.* **2007**, *91*, 231916.
(20) American Society for testing (ASTM)*Terrestrial reference spectra for photovoltaic performance evaluation*, ASTM G173-03, global tilt. http://rredc.nrel.gov/solar/spectra/am1.5/, Online; accessed 6-May-2019.
(21) Tauc, J.; Grigorovici, R.; Vancu, A. Optical properties and electronic structure of amorphous germanium. *Phys. Status Solidi B* **1966**, *15*, 627−637.
(22) Cesaria, M.; Caricato, A. P.; Martino, M. Realistic absorption coefficient of ultrathin films. *J. Opt.* **2012**, *14*, 105701.
(23) Booth, C. H.; Bridges, F. Improved self-absorption correction for fluorescence measurementsof extended X-Ray absorption fine structure. *Phys. Scr.* **2005**, *115*, 202−204.
(24) Rehr, J. J.; Kas, J. J.; Prange, M. P.; Sorini, A. P.; Takimoto, Y.; Vila, F. D. Ab initio theory and calculations of X-ray spectra. *C. R. Phys.* **2009**, *10*, 548−559.
(25) Rehr, J. J.; Kas, J. J.; Vila, F. D.; Prange, M. P.; Jorissen, K. Parameter-free calculations of x-ray spectra with FEFF9. *Phys. Chem. Chem. Phys.* **2010**, *12*, 5503−5513.
(26) Sayers, D. E.; Stern, E. A.; Lytle, F. W. New technique for investigating noncrystalline structures: Fourier analysis of the extended X-Ray absorption fine structure. *Phys. Rev. Lett.* **1971**, *27*, 1204−1207.
(27) Stern, E. A.; Sayers, D. E.; Lytle, F. W. Extended x-ray-absorption fine-structure technique. III. Determination of physical parameters. *Phys. Rev. B* **1975**, *11*, 4836−4846.
(28) Klementev, K. V. K. V. Extraction of the fine structure from x-ray absorption spectra. *J. Phys. D: Appl. Phys.* **2001**, *34*, 209−217.
(29) Momma, K.; Izumi, F. VESTA 3 for three-dimensional visualization of crystal, volumetric and morphology data. *J. Appl. Crystallogr.* **2011**, *44*, 1272−1276.
(30) Sakai, M.; Kontani, T.; Nakamura, O.; Takeyama, K.; Uwatoko, Y.; Obi, Y.; Takanashi, K. Electrical transport and optical properties of hydrogen-deficient YH_2 films. *Jpn. J. Appl. Phys.* **2004**, *43*, 681−687.
(31) Stenzel, O. *The physics of thin film optical spectra*; 2005; pp 107−124.
(32) Broux, T.; Ubukata, H.; Pickard, C. J.; Takeiri, F.; Kobayashi, G.; Kawaguchi, S.; Yonemura, M.; Goto, Y.; Tassel, C.; Kageyama, H. High-pressure polymorphs of LaHO with anion coordination. *J. Am. Chem. Soc.* **2019**, *141*, 8717−20.
(33) Nagengast, D. G.; Kerssemakers, J. W. J.; van Gogh, A. T. M.; Dam, B.; Griessen, R. Epitaxial switchable yttrium-hydride mirrors. *Appl. Phys. Lett.* **1999**, *75*, 1724−1726.
(34) Adachi, G.; Imanaka, N. The binary rare earth oxides. *Chem. Rev.* **1998**, *98*, 1479−1514.
(35) Zinkevich, M. Thermodynamics of rare earth sesquioxides. *Prog. Mater. Sci.* **2007**, *52*, 597−647.
(36) Borowski, M. Size determination of small Cu-clusters by EXAFS. *J. Phys. IV* **1997**, *7*, C2-259.
(37) Michmerhuizen, A.; Rose, K.; Annankra, W.; Vander Griend, D. A. Radius ratio rule rescue. *J. Chem. Educ.* **2017**, *94*, 1480.
(38) Eder, R.; Pen, H. F.; Sawatzky, G. A. Kondo-lattice like effects of hydrogen in transition metals. *Phys. Rev. B: Condens. Matter Mater. Phys.* **1997**, *56*, 10115−10120.
(39) Ng, K. K.; Zhang, F. C.; Anisimov, V. I.; Rice, T. M. Theory for metal hydrides with switchable optical properties. *Phys. Rev. B: Condens. Matter Mater. Phys.* **1999**, *59*, 5398−5413.
(40) Kato, D.; Hongo, K.; Maezono, R.; Higashi, M.; Kunioku, H.; Yabuuchi, M.; Suzuki, H.; Okajima, H.; Zhong, C.; Nakano, K.; Abe, R.; Kageyama, H. Valence band engineering of layered bismuth oxyhalides toward stable visible-light water splitting: Madelung site potential analysis. *J. Am. Chem. Soc.* **2017**, *139*, 18725−18731.
(41) Zapp, N.; Auer, H.; Kohlmann, H. YHO, an air-stable ionic hydride. *Inorg. Chem.* **2019**, *58*, 14635−14641.
(42) Yamashita, H.; Broux, T.; Kobayashi, Y.; Takeiri, F.; Ubukata, H.; Zhu, T.; Hayward, M. A.; Fujii, K.; Yashima, M.; Shitara, K.; Kuwabara, A.; Murakami, T.; Kageyama, H. Chemical pressure-induced anion order-disorder transition in LnHO enabled by hydride size flexibility. *J. Am. Chem. Soc.* **2018**, *140*, 11170−11173.
(43) Ubukata, H.; Broux, T.; Takeiri, F.; Shitara, K.; Yamashita, H.; Kuwabara, A.; Kobayashi, G.; Kageyama, H. Hydride conductivity in an anion-ordered fluorite structure LnHO with an enlarged bottleneck. *Chem. Mater.* **2019**, *31*, 7360−7366.
(44) Pishtshev, A.; Strugovshchikov, E.; Karazhanov, S. Conceptual design of yttrium oxyhydrides: phase diagram, structure, and properties. *Cryst. Growth Des.* **2019**, *19*, 2574−2582.
(45) Maehlen, J. P.; Mongstad, T. T.; You, C. C.; Karazhanov, S. Lattice contraction in photochromic yttrium hydride. *J. Alloys Compd.* **2013**, *580*, S119−S121.

https://dx.doi.org/10.1021/acs.jpcc.0c02410
J. Phys. Chem. C 2020, 124, 13541−13549